Erbium-doped spiral amplifiers with 20 dB of net gain on silicon

Sergio A. Vázquez-Córdova,[1,2,*] Meindert Dijkstra,[1,2] Edward H. Bernhardi,[1] Feridun Ay,[1,3] Kerstin Wörhoff,[1] Jennifer L. Herek,[2] Sonia M. García-Blanco,[1,2] and Markus Pollnau[1,4]

[1]*Integrated Optical MicroSystems Group, MESA + Institute for Nanotechnology, University of Twente, P.O. Box 217, 7500 AE Enschede, The Netherlands*

[2]*Optical Sciences Group, MESA + Institute for Nanotechnology, University of Twente, P.O. Box 217, 7500 AE Enschede, The Netherlands*

[3]*Department of Electrical and Electronics Engineering, Anadolu University, 26555 Eskişehir, Turkey*

[4]*Department of Materials and Nano Physics, School of Information and Communication Technology, KTH–Royal Institute of Technology, Electrum 229, Isafjordsgatan 22–24, 16440 Kista, Sweden*

[*]*s.a.vazquezcordova-1@utwente.nl*

Abstract: Spiral-waveguide amplifiers in erbium-doped aluminum oxide on a silicon wafer are fabricated and characterized. Spirals of several lengths and four different erbium concentrations are studied experimentally and theoretically. A maximum internal net gain of 20 dB in the small-signal-gain regime is measured at the peak emission wavelength of 1532 nm for two sample configurations with waveguide lengths of 12.9 cm and 24.4 cm and concentrations of 1.92×10^{20} cm^{-3} and 0.95×10^{20} cm^{-3}, respectively. The noise figures of these samples are reported. Gain saturation as a result of increasing signal power and the temperature dependence of gain are studied.

OCIS codes: (130.0130) Integrated optics; (140.4480) Optical amplifiers; (160.5690) Rare-earth-doped materials; (130.2755) Glass waveguides.

References and links

1. R. Soulard, A. Zinoviev, J. L. Doualan, E. Ivakin, O. Antipov, and R. Moncorgé, "Detailed characterization of pump-induced refractive index changes observed in Nd:YVO_4, Nd:$GdVO_4$ and Nd:KGW," Opt. Express **18**(2), 1553–1568 (2010).
2. J. D. B. Bradley, M. Costa e Silva, M. Gay, L. Bramerie, A. Driessen, K. Wörhoff, J. C. Simon, and M. Pollnau, "170 Gbit/s transmission in an erbium-doped waveguide amplifier on silicon," Opt. Express **17**(24), 22201–22208 (2009).
3. S. Blaize, L. Bastard, C. Cassagnetes, and J. E. Broquin, "Multiwavelengths DFB waveguide laser arrays in Yb-Er codoped phosphate glass substrate," IEEE Photon. Technol. Lett. **15**(4), 516–518 (2003).
4. E. H. Bernhardi, H. A. van Wolferen, L. Agazzi, M. R. Khan, C. G. Roeloffzen, K. Wörhoff, M. Pollnau, and R. M. de Ridder, "Ultra-narrow-linewidth, single-frequency distributed feedback waveguide laser in Al_2O_3:Er^{3+} on silicon," Opt. Lett. **35**(14), 2394–2396 (2010).
5. D. Geskus, S. Aravazhi, S. M. García-Blanco, and M. Pollnau, "Giant optical gain in a rare-earth-ion-doped microstructure," Adv. Mater. **24**(10), OP19–OP22 (2012).
6. Y. C. Yan, A. J. Faber, H. de Waal, P. G. Kik, and A. Polman, "Erbium-doped phosphate glass waveguide on silicon with 4.1 dB/cm gain at 1.535 μm," Appl. Phys. Lett. **71**(20), 2922–2924 (1997).
7. L. H. Slooff, M. J. A. de Dood, A. van Blaaderen, and A. Polman, "Effects of heat treatment and concentration on the luminescence properties of erbium-doped silica sol-gel films," J. Non-Cryst. Solids **296**(3), 158–164 (2001).
8. J. Yang, M. B. J. Diemeer, D. Geskus, G. Sengo, M. Pollnau, and A. Driessen, "Neodymium-complex-doped photodefined polymer channel waveguide amplifiers," Opt. Lett. **34**(4), 473–475 (2009).
9. K. Wörhoff, J. D. B. Bradley, F. Ay, D. Geskus, T. P. Blauwendraat, and M. Pollnau, "Reliable low-cost fabrication of low-loss Al_2O_3:Er^{3+} waveguides with 5.4-dB optical gain," IEEE J. Quantum Electron. **45**(5), 454–461 (2009).
10. L. Agazzi, J. D. B. Bradley, M. Dijkstra, F. Ay, G. Roelkens, R. Baets, K. Wörhoff, and M. Pollnau, "Monolithic integration of erbium-doped amplifiers with silicon-on-insulator waveguides," Opt. Express **18**(26), 27703–27711 (2010).

#221324 - $15.00 USD Received 19 Aug 2014; revised 24 Sep 2014; accepted 3 Oct 2014; published 15 Oct 2014

11. E. Delevaque, T. Georges, M. Monerie, P. Lamouler, and J. F. Bayon, "Modeling of pair-induced quenching in erbium-doped silicate fibers," IEEE Photon. Technol. Lett. **5**(1), 73–75 (1993).
12. R. Paschotta, J. Nilsson, P. R. Barber, J. E. Caplen, A. C. Tropper, and D. C. Hanna, "Lifetime quenching in Yb-doped fibers," Opt. Commun. **136**(5–6), 375–378 (1997).
13. L. Agazzi, K. Wörhoff, and M. Pollnau, "Energy-transfer-upconversion models, their applicability and breakdown in the presence of spectroscopically distinct ion classes: A case study in amorphous $Al_2O_3:Er^{3+}$," J. Phys. Chem. C **117**(13), 6759–6776 (2013).
14. J. Shmulovich, "Er-doped glass waveguide amplifiers on silicon," in: Rare-Earth-Doped Devices, Proc. SPIE **2996** (San José, CA, 1997), pp. 143–153.
15. P. G. Kik and A. Polman, "Cooperative upconversion as the gain-limiting factor in Er doped miniature Al_2O_3 optical waveguide amplifiers," J. Appl. Phys. **93**(9), 5008–5012 (2003).
16. F. D. Patel, S. DiCarolis, P. Lum, S. Venkatesh, and J. N. Miller, "A compact high-performance optical waveguide amplifier," IEEE Photon. Technol. Lett. **16**(12), 2607–2609 (2004).
17. G. Della Valle, S. Taccheo, G. Sorbello, E. Cianci, V. Foglietti, and R. Laporta, "Compact high gain erbium-ytterbium doped waveguide amplifier fabricated by Ag-Na ion exchange," Electron. Lett. **42**(11), 632–633 (2006).
18. J. Yang, K. van Dalfsen, K. Wörhoff, F. Ay, and M. Pollnau, "High-gain $Al_2O_3:Nd^{3+}$ channel waveguide amplifiers at 880 nm, 1060 nm, and 1330 nm," Appl. Phys. B **101**(1–2), 119–127 (2010).
19. S. Uhlig and M. Robertsson, "Limitations to and solutions for optical loss in optical backplanes," J. Lightwave Technol. **24**(4), 1710–1724 (2006).
20. L. Dellmann, C. Berger, R. Beyeler, R. Dangel, M. Gmür, R. Hamelin, F. Horst, T. Lamprecht, N. Meier, T. Morf, S. Oggioni, M. Spreafico, R. Stevens, and B. J. Offrein, "120 Gb/s optical card-to-card interconnect link demonstrator with embedded waveguides," in *Proc. 57th Electronic Components and Technology Conference* (Reno, NV, 2007), pp. 1288–1293.
21. J. Yang, T. Lamprecht, K. Wörhoff, A. Driessen, F. Horst, B. J. Offrein, F. Ay, and M. Pollnau, "Integrated optical backplane amplifier," IEEE J. Sel. Top. Quantum Electron. **17**(3), 609–616 (2011).
22. J. D. B. Bradley and M. Pollnau, "Erbium-doped integrated waveguide amplifiers and lasers," Laser Photonics Rev. **5**(3), 368–403 (2011).
23. J. D. B. Bradley, L. Agazzi, D. Geskus, F. Ay, K. Wörhoff, and M. Pollnau, "Gain bandwidth of 80 nm and 2 dB/cm peak gain in $Al_2O_3:Er^{3+}$ optical amplifiers on silicon," J. Opt. Soc. Am. B **27**(2), 187–196 (2010).
24. J. D. B. Bradley, F. Ay, K. Wörhoff, and M. Pollnau, "Fabrication of low-loss channel waveguides in Al_2O_3 and Y_2O_3 layers by inductively coupled plasma reactive ion etching," Appl. Phys. B **89**(2–3), 311–318 (2007).
25. G. N. van den Hoven, R. J. I. M. Koper, A. Polman, C. van Dam, J. W. M. van Uffelen, and M. K. Smit, "Net optical gain at 1.53 μm in Er-doped Al_2O_3 waveguides on silicon," Appl. Phys. Lett. **68**(14), 1886–1888 (1996).
26. B. V. Phoenix, http://www.phoenixbv.com/.
27. J. D. B. Bradley, "$Al_2O_3:Er^{3+}$ as a gain platform for integrated optics," Ph.D. Thesis, University of Twente, The Netherlands (2009).
28. Y. Okamura, S. Yoshinaka, and S. Yamamoto, "Measuring mode propagation losses of integrated optical waveguides: a simple method," Appl. Opt. **22**(23), 3892–3894 (1983).
29. H. Schober, D. Strauch, and B. Dorner, "Lattice dynamics of sapphire (Al_2O_3)," Z. Phys. B Condens. Matter **92**(3), 273–283 (1993).
30. L. Agazzi, K. Wörhoff, A. Kahn, M. Fechner, G. Huber, and M. Pollnau, "Spectroscopy of upper energy levels in an Er^{3+}-doped amorphous oxide," J. Opt. Soc. Am. B **30**(3), 663–677 (2013).
31. G. P. Agrawal, *Fiber-Optic Communications Systems*, (John Wiley & Sons, Inc., 2002), ch. 6.
32. N. Kagi, A. Oyobe, and K. Nakamura, "Temperature dependence of the gain in erbium-doped fibers," J. Lightwave Technol. **9**(2), 261–265 (1991).

1. Introduction

Rare-earth-ion-doped materials are of high interest as amplifiers and lasers in integrated optics. Their significantly longer excited-state lifetime and weaker refractive-index change ($\Delta n \sim 10^{-6}$) induced by the excitation of rare-earth ions [1], both compared to electron-hole pairs in III-V semiconductors, provide spatially and temporally stable optical gain, allowing for high-speed amplification [2] and narrow-linewidth lasers [3,4]. Highly rare-earth-ion-doped crystalline materials can provide optical gain per unit length of ~1000 dB/cm [5], making them competitive with waveguide amplifiers in III-V semiconductors. However, neither of these two material classes can easily be integrated on a silicon chip. Rare-earth-ion-doped amorphous materials can be monolithically integrated [6–9] on a number of passive photonic platforms, including silicon-on-insulator (SOI) [10]. Unfortunately, inhomogeneous linewidth broadening diminishes the transition cross-sections of rare-earth ions in this class of materials. Besides, parasitic spectroscopic processes such as migration-accelerated energy-transfer upconversion (ETU) among rare-earth ions can counteract the establishment of high

#221324 - $15.00 USD Received 19 Aug 2014; revised 24 Sep 2014; accepted 3 Oct 2014; published 15 Oct 2014

inversion. Moreover, fast quenching processes originating in static ETU among active ion pairs or clusters, energy transfer to undesired impurities, or trapping of excitation energy by host material defects, such as voids, may further reduce the available gain [11–13]. Consequently, gain per unit length of only up to ~10 dB/cm has been reported so far [14–18]. Whereas the resulting amplifier lengths of several to many centimeters required to achieve sufficient pump absorption and overall signal gain, often necessitating spiral designs [15], may render such devices unsuitable for very-large-scale integration, other applications allowing for more space per device, such as amplification in optical printed circuit boards (OPCBs) [19–21], may well profit from this approach.

Among the many materials for Er^{3+}-doped integrated waveguide amplifiers and lasers around 1.5 μm [22], amorphous Al_2O_3:Er^{3+} exhibits remarkable performance [23]. The waveguide amplifiers are realized by RF reactive co-sputtering of the material onto thermally oxidized silicon wafers [9] followed by optical lithography and chlorine-based reactive ion etching for the definition of low-loss channel waveguides [24]. A peak gain per unit length of 2 dB/cm at 1533 nm and a gain bandwidth of 80 nm have been demonstrated [23]. The gain is limited by migration-accelerated ETU from the $^4I_{13/2}$ gain level and a fast quenching process [13]. A theoretical model has been proposed, in which these processes are taken into consideration, permitting the design of on-chip waveguide amplifiers [13].

In this work, we experimentally verify the previously proposed theoretical model [13], which is utilized to design spiral channel waveguide amplifiers in Al_2O_3:Er^{3+}. Several devices varying the Er^{3+} dopant concentration and spiral length are fabricated and characterized. A comparison of the experimental results with the theoretical model is presented. A small-signal gain of 20 dB at 1532 nm is demonstrated for two sample configurations with waveguide lengths of 12.9 cm and 24.4 cm and concentrations of 1.92×10^{20} cm^{-3} and 0.95×10^{20} cm^{-3}, respectively. This achievement improves previous results in this host material of 2.3 dB [25], 5.4 dB [9], and 9.3 dB [23] by a factor of 9, 3.7, and 2.2, respectively.

2. Amplifier design and fabrication

Important design parameters for the optimization of a waveguide amplifier are the pump wavelength, the launched pump power, the geometrical waveguide cross-section providing fundamental-mode operation at both the pump and signal wavelengths, a good overlap of pump and signal modes with each other and with the active area, the dopant concentration, the amplifier length, and the waveguide propagation loss at the pump and, more importantly, the signal wavelength.

Stimulated emission on the pump transition $^4I_{15/2} \leftrightarrow {}^4I_{13/2}$ at 1480 nm plays a more significant role than on the pump transition $^4I_{15/2} \leftrightarrow {}^4I_{11/2}$ at 980 nm because of the significantly longer lifetime and, consequently, larger population density of the $^4I_{13/2}$ compared to the $^4I_{11/2}$ level. This fact governed our choice of the 976 nm pump wavelength.

Mode-field simulations at the pump and signal wavelengths were carried out using the Finite Difference (FD) algorithm in the *Phoenix Field Designer* software [26]. The waveguide cross-section consisted of a 1-μm-thick by 1.5-μm-wide Al_2O_3:Er^{3+} channel with ridge height of 0.35 μm [Fig. 1 (a)]. This geometry allows high confinement in straight and bent sections of the waveguide. Moreover, higher signal and pump intensities are achieved in comparison with the channel geometry presented by Bradley *et al.* [23]. The simulated pump and signal mode fields had an overlap of ~95% and ~85% with the doped region, respectively. The refractive indices employed in the simulations were taken from previous measurements [27]. The waveguide cross-section and the mode-field distribution at the signal wavelength of 1532 nm are displayed in Fig. 1(a).

#221324 - $15.00 USD Received 19 Aug 2014; revised 24 Sep 2014; accepted 3 Oct 2014; published 15 Oct 2014

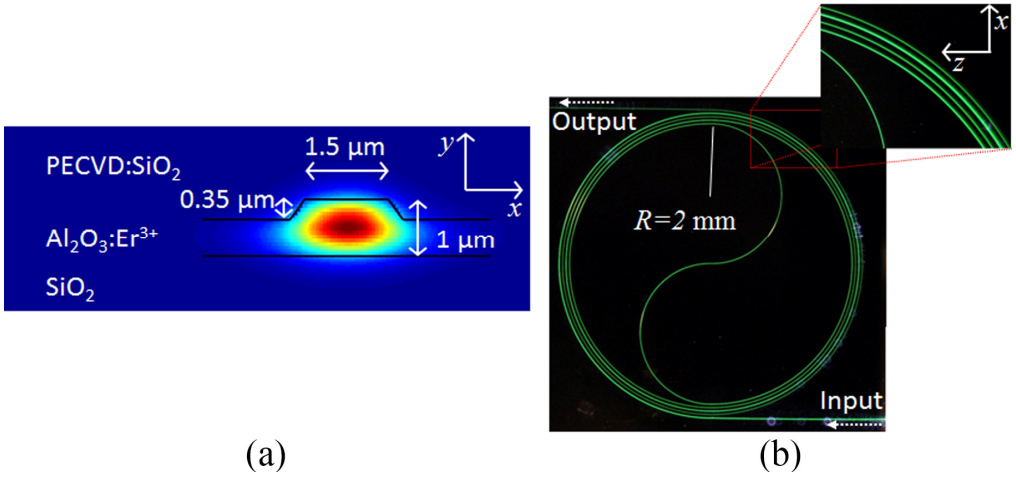

Fig. 1. (a) Waveguide amplifier cross-section and simulated signal-mode profile. (b) Photograph of a pumped (λ_P = 976 nm) $Al_2O_3:Er^{3+}$ spiral amplifier on a silicon chip. A close-up view of the spiral amplifier is shown in the inset.

Understanding the performance of an Er^{3+}-doped amplifier is significantly complicated by the spectroscopic processes of the Er^{3+} ion. The migration-accelerated ETU process ($^4I_{13/2}$, $^4I_{13/2}$) → ($^4I_{15/2}$, $^4I_{9/2}$) induces a concentration- and excitation-dependent quenching of the $^4I_{13/2}$ amplifier level. More importantly, a fast quenching process of this level occurs in SiO_2 [11], $Al_2O_3:Er^{3+}$ [13], and potentially other Er^{3+}-doped materials, which limits the optimum Er^{3+} concentration in Al_2O_3 to 1–2 × 10^{20} cm^{-3}. As a consequence, waveguide lengths on the order of 10 cm are desired for efficient amplifier performance.

Al_2O_3 layers with Er^{3+} concentrations of 0.45 × 10^{20} cm^{-3}, 0.95 × 10^{20} cm^{-3}, 1.92 × 10^{20} cm^{-3}, and 3.0 × 10^{20} cm^{-3} were deposited onto thermally oxidized silicon substrates by RF reactive co-sputtering [9]. For each of the four different doping concentrations, spiral-shaped channel waveguides with different lengths varying from 12.9 cm to 41.6 cm were patterned into the $Al_2O_3:Er^{3+}$ layers using standard lithographic techniques and chlorine-based reactive ion etching [24]. The spiral shape [Fig. 1(b)] minimizes the device foot print. A minimum bending radius of R = 2 mm was selected. For this radius, the simulated additional bending loss of $<10^{-6}$ dB/cm is negligible compared to the straight-waveguide propagation loss of ~0.1 dB/cm and the mode-mismatch loss of ~0.02 dB at the junction in the center of the spiral. Transverse-electric (TE) polarization was chosen for signal and pump light in the simulations and measurements.

A 5-µm-thick SiO_2 layer was deposited on top of each patterned Al_2O_3 layer by PECVD as a protective cladding. Finally, waveguide end faces were prepared by dicing.

3. Propagation losses

The non-destructive method proposed by Okamura *et al.* [28] was applied to investigate the propagation loss in our devices. The method consists of capturing a top-view image (InGaAs camera Sensors Inc. SU320M-1.7RT, 320 × 240 px.) of the infrared light (λ = 1320 nm, Amoco laser model D200) scattered from a quarter of the spiral waveguide, as shown in Fig. 2(a). The wavelength selected for this experiment lies outside the Er^{3+} absorption bands and, thus, the passive characteristics can be determined. Background propagation losses around 1530 nm are expected to be similar to those at 1320 nm and 0.18 dB/cm higher at 980 nm due to Rayleigh scattering [23]. A spatial calibration of the image was readily performed, since the dimensions of the spirals are well known from the lithographic mask. It was assumed that in average the intensity of scattered light is proportional to the intensity of light propagating within the channel. This is the case if the scattering centers (such as channel interface

#221324 - $15.00 USD Received 19 Aug 2014; revised 24 Sep 2014; accepted 3 Oct 2014; published 15 Oct 2014

roughness) are uniformly distributed along the waveguide channel. It is then possible to correlate the intensity distribution of scattered light along the channel to the propagation length by the Lambert-Beer law when the propagation direction and the spiral dimensions are known. Only one quarter of the spiral [the top right quarter displayed in Fig. 1(b)] was imaged during the measurements, because the other three quarters were affected by scattered stray light coupled into the slab waveguide, which made those measurements less accurate. Nevertheless, by analyzing only a single quarter, the remaining three quarters are intrinsically evaluated due to the spiral shape of the waveguide. Thus, any defect causing a probe-signal loss in the channel waveguide outside the captured area is observed as a drop in intensity in one of the channels of the inspected quarter.

A MATLAB code was written for analysis of the intensity profiles. In the code, the intensity profiles were selected along the circular paths of the channels. The intensity profile of each selected channel was integrated radially and plotted in a logarithmic scale along the light-propagation direction, see Fig. 2(b). A linear fit to the experimental data [Fig. 2(b)] is shown as a continuous line, and its slope provides the propagation-loss coefficient in dB/cm, which was averaged over three independent measurements of the same spiral quarter.

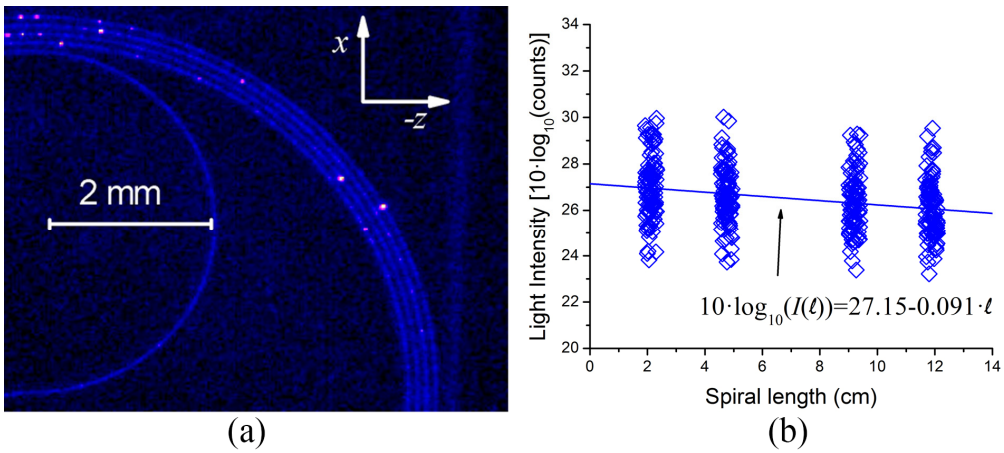

Fig. 2. (a) Infrared image (λ = 1320 nm) of a quarter of a spiral-shaped channel waveguide. (b) Intensity distribution along the propagation direction in the spiral-shaped channel waveguide measured by applying the imaging method described in [28].

Background propagation losses (α_{loss}) derived from the fits were found to be in average 0.19 dB/cm within the range of 0.08−0.41 dB/cm. These results are similar to those reported by Bradley *et al.* [23]. Variations between individual spirals are attributed to limitations in the sputtering and lithographic processes. Defects caused by residual resist and layer defects over or close to the channels increased the scattering and appeared as bright spots along the waveguides, see Fig. 2(a).

For the gain measurements, a fiber-based wavelength division multiplexer (WDM) was employed to combine (split) and launch (collect) the pump and signal. One of the WDM ports was used to launch a probe signal for the insertion-loss measurements. This enabled us to maintain the same fiber-waveguide-fiber alignment in the gain and insertion-loss measurements. Total insertion losses were measured to estimate the coupling loss right after each gain measurement. A probe signal scanned in the wavelength range from 1630 nm to 1640 nm was launched into the input end-facet of the waveguide. Potential errors in insertion-loss measurements, caused by destructive interference due to reflections at the fiber end facet and the chip front facet when launching highly coherent light, can be reduced by launching probe signals at different wavelengths. A second fiber-based WDM with the same characteristics as the launching, aligned to the output end-facet of the spiral, collected the

#221324 - $15.00 USD Received 19 Aug 2014; revised 24 Sep 2014; accepted 3 Oct 2014; published 15 Oct 2014

transmitted signal. The coupling loss was calculated by subtracting the previously determined propagation loss from the total insertion loss. The Al_2O_3:Er^{3+} absorption cross-section in the 1630–1640 nm range is very low [23], however the corresponding absorption was considered in the calculations. Since the launching and collecting fibers have exactly the same characteristics, and index-matching-fluid (Diphenyl ether) was used in between fiber and waveguide facets during all the experiments, it was assumed that similar coupling efficiencies were achieved in both the input and output ports.

4. Optical gain

The pump-and-probe method was applied to measure the internal net gain in the Er^{3+}-doped channel waveguides. The setup consisted of a fiber-pigtailed diode laser operating at 976 nm as the pump source. All gain measurements were performed at a signal wavelength of 1532 nm. The pump and signal light were combined by a fiber-based WDM, which was butt-coupled to the waveguide. Using a second WDM, the transmitted pump power was separated from the amplified signal, which was either investigated by an optical spectrum analyzer (OSA) or detected by an InGaAs detector. The signal was modulated at 280 Hz for lock-in amplification to remove the residual pump power and the amplified spontaneous emission (ASE) from the measured signal. The signal intensities $I_p(\lambda)$ and $I_u(\lambda)$ in the pumped and unpumped case, respectively, were measured at the output fiber. The internal net gain $G(\lambda)$ was then calculated using the equation

$$G(\lambda) = 10\log_{10}\left[I_p(\lambda)/I_u(\lambda)\right] - \alpha_{abs}(\lambda)\ell - \alpha_{loss}(\lambda)\ell, \qquad (1)$$

where $\alpha_{abs}(\lambda)$ is the absorption coefficient of Er^{3+} in dB/cm, $\alpha_{loss}(\lambda)$ is the propagation-loss coefficient in dB/cm obtained from the previous section, and λ is the length of each channel in cm. During the gain measurements ~250 mW of pump power were incident on the channel. Fiber-chip coupling efficiencies on the order of ~10% were estimated.

4.1 Small-signal gain

The incident signal power was set to approximately 1 μW to assure that the measurements were performed in the small-signal-gain regime. The results of small-signal-gain measurements in 23 spiral-shaped waveguide amplifiers of different lengths with doping concentrations of 0.45×10^{20} cm^{-3}, 0.95×10^{20} cm^{-3}, 1.92×10^{20} cm^{-3}, and 3.0×10^{20} cm^{-3} are presented in Fig. 3 as Series A, B, C, and D, respectively. One defective device was identified in each sample series A and C. In both cases, inspection with a microscope verified a large defect in contact with the waveguide channel, see Fig. 4(a), which probably is residual photoresist. These defects cause a strong scattering of pump and signal light, as can be seen from the significant drop in green upconversion luminescence in all waveguide regions following the defect, see Fig. 4(b), thereby substantially reducing the gain. For reference, the gain results of these devices are presented as cross symbols in Fig. 3. Those devices whose combination of dopant concentration and waveguide length led to an almost complete absorption of pump power and accordingly strong reabsorption in the rear unpumped part of the waveguide, resulting in negative net gain of < −20 dB, were not included in the plots.

An internal net gain of ~20 dB was measured for the 24.5-cm-long sample with an Er^{3+} concentration of 0.95×10^{20} cm^{-3} and for the 12.9-cm-long sample with an Er^{3+} concentration of 1.92×10^{20} cm^{-3}. Samples with a smaller concentration-length product exhibited a lower gain because of insufficient pump absorption. Samples with a higher product exhibited increasing reabsorption of the signal in the rear part of the waveguide due to insufficient population inversion, hence lower gain. Moreover, samples with a concentration higher than 3.0×10^{20} cm^{-3} generally showed inferior performance due to an increased fraction of quenched ions, as previously predicted [13].

#221324 - $15.00 USD Received 19 Aug 2014; revised 24 Sep 2014; accepted 3 Oct 2014; published 15 Oct 2014

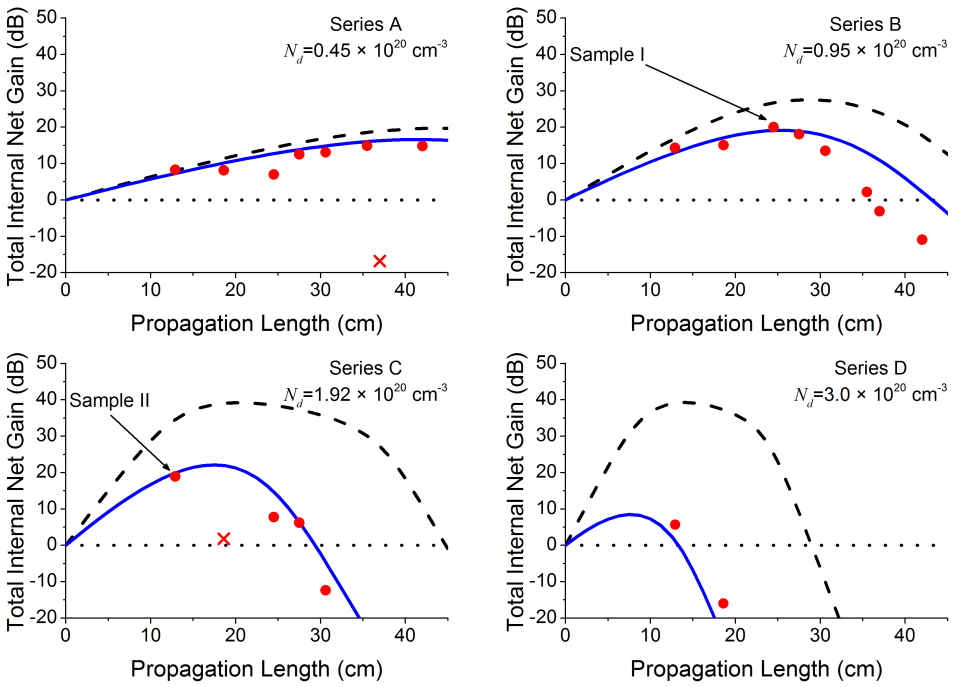

Fig. 3. Internal net gain in Al_2O_3:Er^{3+} spiral waveguide amplifiers: simulations with (solid blue curves) and without (dashed black curves) considering the fraction of quenched ions, and measurements (red circles) for different waveguide lengths and Er^{3+} concentrations of 0.45 × 10^{20} cm^{-3} (Series A), 0.95 × 10^{20} cm^{-3} (Series B), 1.92 × 10^{20} cm^{-3} (Series C), and 3.0 × 10^{20} cm^{-3} (Series D). Simulations are based on the quenched-ion amplifier model [13] and the parameters given in Table 1.

Fig. 4. (a) Defect in contact with the waveguide. (b) Drop of green upconversion luminescence as a result of pump power scattered at the defect location (red circle).

Compared to the highest gain that has previously been reported, ~9.3 dB in the small-signal-gain regime [23], the pump wavelength, typical waveguide propagation losses, optimum range of dopant concentrations, and measured gain per unit length are similar. The improvement achieved in this work stems from the different waveguide cross-section, which is smaller by a factor of three (1.0 × 1.5 μm^2 compared to 1.1 × 4.0 μm^2), and the significantly larger etch depth (350 nm compared to 43–99 nm). These parameters result in similar waveguide propagation losses and simultaneously accept smaller bending radii, thereby allowing for exploitation of the spiral design that provides the longer waveguide lengths that are necessary to achieve 20 dB of optical gain.

#221324 - $15.00 USD Received 19 Aug 2014; revised 24 Sep 2014; accepted 3 Oct 2014; published 15 Oct 2014

4.2 Gain calculation

The amplifier model utilized here [13] accounts for the fractions f_a and f_q of active and quenched ions, respectively, and is based on the following steady-state rate equations:

$$\frac{dN_{2,a/q}}{dt} = R_{P,a/q} + W_{ETU} N_{1,a/q}^2 - \frac{1}{\tau_2} N_{2,a/q} = 0, \tag{2}$$

$$\frac{dN_{1,a/q}}{dt} = -R_{S,a/q} - 2W_{ETU} N_{1,a/q}^2 + \frac{1}{\tau_2} N_{2,a/q} - \frac{1}{\tau_{1,a/q}} N_{1,a/q} = 0, \tag{3}$$

$$f_{a/q} N_d = N_{0,a/q} + N_{1,a/q} + N_{2,a/q}, \tag{4}$$

$$R_{P,a/q} = \frac{\lambda_P}{hc} I_P \left[\sigma_{a,P} N_{0,a/q} - \sigma_{e,P} N_{2,a/q} \right], \tag{5}$$

$$R_{S,a/q} = \frac{\lambda_S}{hc} I_S \left[\sigma_{e,S} N_{1,a/q} - \sigma_{a,S} N_{0,a/q} \right]. \tag{6}$$

Here, N_i is the population density of level i = 0, 1, or 2, representing the Er^{3+} level $^4I_{15/2}$, $^4I_{13/2}$, or $^4I_{11/2}$, respectively, where the subscripts a/q denote the active or quenched ions. $R_{P,a/q}$ is the pump rate, and $R_{S,a/q}$ is the signal rate. I_P and I_S are the pump and signal intensities, respectively. τ_i is the intrinsic luminescence lifetime of excited level i. The intrinsic luminescence lifetime of the Er^{3+} $^4I_{13/2}$ upper level of the amplifier transition is τ_{1a} = 7.55 ms for the active ions. The decay rate from this level is increased by ETU. W_{ETU} is the macroscopic parameter accounting for the migration-accelerated ETU process ($^4I_{13/2}$, $^4I_{13/2}$) → ($^4I_{15/2}$, $^4I_{9/2}$), defined by the donor-donor and donor-acceptor micro-parameters C_{DD} and C_{DA} of migration and ETU, respectively, and the Er^{3+} doping concentration N_d as [13]

$$W_{ETU} = \frac{\pi^2}{3} \sqrt{C_{DD} C_{DA}} N_d. \tag{7}$$

Besides intrinsic decay and ETU, the concentration-dependent fraction f_q of Er^{3+} ions undergoes a fast quenching process, which may be caused by, e.g., static ETU among active ion pairs or clusters, energy transfer to undesired impurities, or trapping of excitation energy by host material defects, such as voids, resulting in a lifetime τ_{1q} on the order of, or even less than, 1 μs [13]. The model does not take into account higher energy levels of Er^{3+}, because the high phonon energies (~870 cm^{-1}) [29] in Al_2O_3 induce a fast multiphonon decay to the lower-lying energy levels. Hence, the excitation density of the $^4I_{9/2}$ level that is induced by ETU rapidly decays back to the $^4I_{11/2}$ level via multiphonon relaxation. However, excited-state absorption (ESA) at the pump wavelength on the transition $^4I_{11/2}$ → $^4F_{7/2}$ is considered in the modeling of the pump intensity propagating along the waveguide. It is described by the equation

$$\frac{dP_P(z)}{dz} = P_P(z) \left\{ \iint_{A_{Er}} \Psi_P \left[\sigma_{e,P} N_{2,a/q} - \left(\sigma_{a,P} N_{0,a/q} + \sigma_{ESA,P} N_{2,a/q} \right) \right] dxdy - \alpha_{loss}(\lambda_P) \right\}. \tag{8}$$

$P_P(z)$ is the pump power along the propagation direction z, A_{Er} is the area of the active region, Ψ_P is the normalized mode-profile distribution simulated with Phoenix B.V. software [26], $\alpha_{loss}(\lambda_P)$ is the background propagation loss at the pump wavelength, $\sigma_{e,P/S}$ and $\sigma_{a,P/S}$ are the effective emission and absorption cross-sections for pump and signal, respectively, and $\sigma_{ESA,P}$ is the pump-ESA cross-section [30]. Similarly, the signal power propagating in the waveguide is described by the equation

#221324 - $15.00 USD Received 19 Aug 2014; revised 24 Sep 2014; accepted 3 Oct 2014; published 15 Oct 2014

$$\frac{dP_S(z)}{dz} = P_S(z)\left\{\iint_{A_{Er}} \Psi_S\left[\sigma_{e,S}N_{1,a/q} - \sigma_{a,S}N_{0,a/q}\right]dxdy - \alpha_{loss}(\lambda_S)\right\}, \qquad (9)$$

where $P_S(z)$ is the signal power along the propagation direction z and $\alpha_{loss}(\lambda_S)$ is the background propagation loss at the signal wavelength.

As previously described in section 3, an insertion-loss measurement was carried out immediately after the gain measurement to estimate the coupling efficiency. For the simulation it was assumed that signal and pump wavelengths have similar coupling efficiencies. This assumption is in agreement with the mode-overlap calculation between the simulated mode profiles of the waveguide and the launching and collecting fibers. Due to the small variation (<1%) in refractive index with increasing doping concentration [27] one would expect similar mode-field distributions in the waveguides and, therefore, similar coupling efficiencies for all the samples. Nevertheless, different imperfections at the end faces of each sample were observed and attributed to the dicing finish. These imperfections caused in average a 24% deviation of the coupling efficiency from the theoretical prediction. However, in the gain simulations presented in Fig. 3 a constant coupling efficiency was assumed for each sample series. All values applied in the simulations are presented in Table 1.

Table 1. Parameters and Values Applied to the Gain Simulation. Sources [a] [13], [b] [30], and [c] [23].

Sample series		A	B	C	D
Er^{3+} concentration (10^{20} cm^{-3})	N_d	0.45	0.95	1.92	3.0
Fraction of quenched ions	f_q	4.37% [a]	9.69% [a]	18.6% [a]	29.1% [a]
$^4I_{13/2}$ lifetime of active ions	τ_{1a}	7.55 ms [a]			
$^4I_{13/2}$ lifetime of quenched ions	τ_{1q}	1 µs [a]			
Migration micro-parameter	C_{DD}	5×10^{-39} cm^6/s [a]			
ETU micro-parameter	C_{DA}	1.16×10^{-40} cm^6/s [a]			
ETU macro-parameter (10^{-19} cm^3/s)	W_{ETU}	1.13	2.38	**4.81**	7.52
$^4I_{11/2}$ lifetime	τ_2	60 µs [a]			
Pump wavelength	λ_P	976 nm			
Pump eff. absorption cross-section	$\sigma_{a,P}$	2.01×10^{-21} cm^2 @ 976 nm [b]			
Pump eff. emission cross-section	$\sigma_{e,P}$	1.71×10^{-21} cm^2 @ 976 nm [b]			
Pump ESA cross-section	$\sigma_{ESA,P}$	1.69×10^{-21} cm^2 @ 976 nm [b]			
Signal wavelength	λ_S	1532 nm			
Signal eff. absorption cross-section	$\sigma_{a,S}$	5.65×10^{-21} cm^2 @ 1532 nm [c]			
Signal eff. emission cross-section	$\sigma_{e,S}$	5.65×10^{-21} cm^2 @ 1532 nm [c]			
Incident pump power	$P_{P,inc}$	250 mW			
Incident signal power	$P_{S,inc}$	1 µW			
Coupling efficiency	η_{in}	11%	11%	12%	12%
Propagation loss (dB/cm)	α_{loss}	0.14	0.25	0.17	0.2

Two different simulations of gain versus waveguide length for the four different concentrations are presented in Fig. 3. In both simulations the ETU process is taken into account. In the first case (dashed line) we assume that all Er^{3+} ions are active, whereas in the second case (solid line) we consider that the $^4I_{13/2}$ excitation density of the fraction f_q of ions is quenched. As becomes clear from Fig. 3, only when including the fast quenching process, the measurements can be reproduced with good accuracy. This model also correctly reproduces the gain-saturation results presented in the following subsection and the gain measurements presented in [23], where ~9.3 dB of gain in the small-signal-gain regime was measured for a 5.4-cm-long straight ridge waveguide with a doping concentration similar to that in sample series B. The agreement of the simulations with all the experimental results is a direct consequence of applying the correct values of the transition cross-sections and the ETU parameter and by taking into account the concentration-dependent fraction of quenched ions in the amplifier model [13].

#221324 - $15.00 USD Received 19 Aug 2014; revised 24 Sep 2014; accepted 3 Oct 2014; published 15 Oct 2014

4.3 Gain saturation and power amplification

The small-signal-gain regime provides the maximum gain achievable by an optical amplifier. However, for telecommunication applications stronger signals of ~−10 dBm are required, and usually the optical amplifier works in a saturated-gain regime. Here we investigate the two best performing samples from section 4.2 by applying different incident signal powers. These samples will be referred to as Sample I from sample series B, and sample II from series C. Sample I and II have a waveguide length of 24.45 cm and 12.91 cm, respectively. Experimental and simulated gain results at different launched signal and pump powers are shown in Fig. 5(a) for sample II.

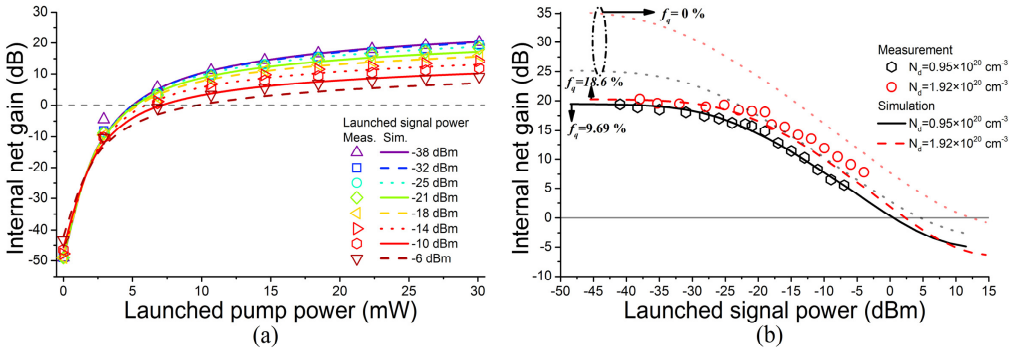

Fig. 5. (a) Measured (symbols) and simulated (curves) internal net gain at different launched signal powers for the 12.9-cm-long spiral waveguide with an Er^{3+} concentration of 1.92 × 10^{20} cm^{-3} at different pump powers. (b) Maximum internal net gain as a function of launched signal power for two samples with concentrations of 0.95 × 10^{20} cm^{-3} (black) and 1.92 × 10^{20} cm^{-3} (red) and lengths of 24.45 and 12.91 cm, respectively. The data points show the measured values, while the continuous, dashed, and dotted curves show the simulated values including and excluding f_q, respectively.

Good agreement between the measured and simulated gain as a function of launched pump power for different signal powers is obtained. As expected, gain saturation is observed as a result of increasing the input-pump power, because a larger fraction of the active ions becomes excited and the ground state is bleached by the increasing pump power, until the waveguide becomes almost transparent at the pump wavelength and an additional increase in pump power does not further improve the gain. Moreover, gain saturation is also observed when increasing the input-signal power, because stimulated emission triggered by the propagating signal photons introduces an additional decay rate of the excited level, thereby reducing the excitation density that is obtained for the same amount of launched pump power. In Fig. 5(b) the gain dependence on the signal power is shown for both samples I and II. The parameters specified in Table 1 were used for the simulation results presented in Fig. 5, except for the coupling efficiency and propagation losses, for which the actual determined values for these two spirals were employed. These were 8% and 16% for the coupling efficiency and 0.16 dB/cm and 0.17 dB/cm for the propagation losses for sample I and II, respectively.

As can be seen from Fig. 5(b), sample I with lower concentration exhibited a slightly inferior performance, caused by the lower coupling efficiency for the same incident signal and pump powers. Thus, the lower pump power available at the rear part of the waveguide caused a smaller population inversion and, therefore, lower gain, which was observed by the lower amount of pump power measured at the waveguide output. In spite of the lower performance observed in sample I, one can presume that lower launched pump powers are required in this configuration to obtain similar gain values. This is a direct consequence of the

#221324 - $15.00 USD Received 19 Aug 2014; revised 24 Sep 2014; accepted 3 Oct 2014; published 15 Oct 2014

larger fraction of quenched ions that is present at higher doping concentrations. When neglecting the fraction of quenched ions, the gain performance is overestimated, as shown by the dotted lines in Fig. 5(b). Net gain was observed in the saturated-gain regime for both samples for launched signal powers in the range of 0.1–0.5 mW, which are typically applied in integrated optical circuits [19]. The output saturation power [31] was −7.75 dBm and −4.27 dBm for sample I and II, respectively.

An OSA was used to measure the signal-to-noise ratio (SNR) of the signal before and after amplification in the small-signal-gain regime. Amplifier-noise figures $F_n = (SNR)_{in} / (SNR)_{out}$ [31] of 3.75 dB and 4.58 dB were determined for sample I and II, which are similar to the typical values of >3 dB [31].

By tapering the waveguide cross-section at the input and output ports, one can increase the overlap between the pump mode-field profiles of the $Al_2O_3:Er^{3+}$ waveguide and the coupling fiber and, thereby, increase the coupled pump power and the overall fiber-chip-fiber efficiency. In a similar fashion, matching the pump and signal mode-field profiles of the $Al_2O_3:Er^{3+}$ waveguide with those of a passive optical circuit based on, e.g., polymer, Si_3N_4, or SOI [10] will be fundamental for optimum amplifier operation in an integrated optical circuit. Since our aim is not the application of this amplifier as a stand-alone device within a fiber-based environment but its direct integration with a passive integrated optical circuit, where its potential advantages over other amplification technologies can be better exploited, we have not optimized the fiber-to-Al_2O_3 coupling efficiency in the present work. For the proof of principle demonstrated here, optimization of the coupling efficiency is not crucial, because high internal net gain is demonstrated and gain saturation is reached already with a launched pump power of ~30 mW.

4.4 Gain dependence on temperature

Small-signal-gain measurements at 1532 nm, as described in section 4.1, were conducted at temperatures from 20°C to 140°C in steps of 10°C. For this study, unlike the other gain measurements, index-matching-fluid was not used due to its low flash point and, therefore, the signal and, more importantly, the pump coupling efficiency were decreased. The shortest spiral waveguide (12.9 cm-long) from sample series B was used in this gain study to compensate for the lower launched pump power and still measure net signal gain.

The sample was placed on a bronze vacuum chuck and a thermal compound (DOW CORNING 340) was employed between the sample and the chuck to guarantee good heat conduction. The temperature of the chuck was controlled using a thermo-electric-controller and monitored additionally at the chuck top surface (where the sample was placed) using a thermo-couple. Results of the internal-net-gain measurements at different temperatures are presented in Fig. 6(a). A linear fit to the gain as a function of temperature resulted in a decrease rate of $-4.05 \times 10^{-3} \pm 2.26 \times 10^{-3}$ dB/°C. The ASE spectrum collected from the output end facet of the pumped spiral waveguide was recorded with an OSA at 17.5 and 142.4°C. The area-normalized ASE spectra in linear scale are shown in Fig. 6(b). A decrease rate of -7.28×10^{-3} dB/°C was determined by taking the values of the ASE spectra at the peak wavelength at both temperatures, which is on the same order of magnitude. A temperature dependence of gain on a ground-state transition is expected from studies in erbium-doped fiber amplifiers (EDFA) [32]. The rather weak dependence of the gain performance on temperature increases the potential for integration of $Al_2O_3:Er^{3+}$ waveguide amplifiers in OPCBs, since no active control of the temperature will be required.

#221324 - $15.00 USD Received 19 Aug 2014; revised 24 Sep 2014; accepted 3 Oct 2014; published 15 Oct 2014

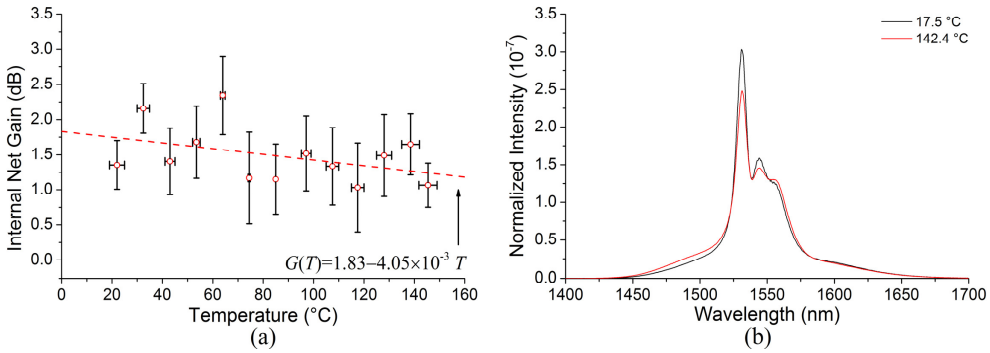

Fig. 6. (a) Measured internal net gain at different sample temperatures for the 12.9-cm-long spiral waveguide with an Er^{3+} concentration of 0.95×10^{20} cm^{-3}. A linear fit is shown as a dashed line. (b) Normalized amplified-spontaneous-emission spectra recorded at 17.5 and 142.4°C.

5. Conclusions

We have presented an experimental study of the amplification characteristics of Er^{3+}-doped aluminum oxide waveguides at 1532 nm and compared the results with a recently established comprehensive model [13]. As predicted, a fast quenching process strongly deteriorates the amplifier performance of the $Al_2O_3:Er^{3+}$ waveguide amplifiers. This effect is accentuated for concentrations higher than 2×10^{20} cm^{-3}. Nevertheless, by carefully choosing the geometrical waveguide cross-section to obtain a large field confinement within the doped region and a good overlap of pump and signal modes, and using correct spectroscopic parameters in the model one can accurately predict and optimize an $Al_2O_3:Er^{3+}$ waveguide amplifier. An internal net gain of 20 dB was measured for two different spiral configurations with waveguide lengths of 12.9 cm and 24.5 cm and Er^{3+} concentrations of 1.92×10^{20} cm^{-3} and 0.95×10^{20} cm^{-3}, respectively. The experimental results confirm the validity of the model developed by Agazzi *et al.* [13], which successfully simulates the characteristics of Er^{3+}-doped aluminum oxide waveguides. Positive net gain was measured in the saturated-gain regime in the range of launched signal powers of 10^{-3}–10^{-1} mW, and the simulations predict that net gain can be achieved up to the mW regime. An amplifier noise figure of 3.75 dB was determined in the small-signal-gain regime. A weak temperature dependence of the gain was measured in the small-signal-gain regime at 1532 nm in the temperature range from 20°C to 140°C.

Acknowledgments

This work was supported by the Dutch Technology Foundation (STW) within the framework of project No. 11689. Sergio A. Vázquez-Córdova gratefully acknowledges CONACyT for its partial scholarship support of his postgraduate studies.